Journal of Marine Research, 68, 387–412, 2010

Depth-integrated steric height as a tool for detecting non-Sverdrup behavior in the global ocean

by J. Stuart Godfrey[1,2] and Jeff R. Dunn[1]

ABSTRACT

Godfrey's (1989) (referred to below as G89) calculation of the global field of annual mean Depth-Integrated Steric Height, or Sverdrup *et al.*'s (1942) "Transport Function," (Q) is revisited, using newer products for wind stresses, temperature and salinity. Observed Q and its wind-estimated equivalent Q_W are compared more extensively along eastern oceanic boundaries than in G89. Q and Q_W are also compared along the inner edge of the Pacific western boundary, at locations where G89 theory suggests that such a comparison is possible. A similar comparison along the western Atlantic improves after a 16 Sv correction for the supply of North Atlantic Deep Water. The observed circumpolar zero contour of Q is used to define an "ACC boundary." South of it, G89 fails grossly as expected. North of the boundary in each ocean basin, a "tongue" of high Q, about 1000 km wide, extends much farther eastward from its western boundary source than in comparable features in the northern hemisphere. The uninterrupted existence of this tongue across the full width of the Indian Ocean occurs because there is no analog in Q to the strong "meridional tip jet" west of southern Tasmania, found in Q_W—i.e. the East Australian Current is weaker in observed Q than predicted by G89. Elsewhere, each MTJ in Q_W does have an analog in observed Q; but the latter jets tend to follow local Sverdrup flow rather than being zonal. A final section provides qualitative discussion of the possible dynamics of these observed departures of Q from Sverdrup balance, north of the ACC.

1. Introduction

Godfrey (1989) displayed a global map of time-averaged Depth-Integrated Steric Height, or "transport function" (Q; Sverdrup *et al.,* 1942; Sverdrup, 1947), from a linear model whose only input data were the observed annual mean wind stresses. When Q is obtained from the wind stress via G89, the symbol Q_w is used below.

Q can also be obtained directly from hydrographic data. The steric height $\eta(p(z),p(Z))$ at depth z relative to a depth of no motion at a greater depth Z is the more familiar "dynamic height," divided by $\rho_0 g$ to give it the actual dimensions of a height. Here and elsewhere, ρ_0 is a nominal water density of about 1028 kg/m^3. $p(z)$ is the measured pressure; to Boussinesq approximation, $p(z) = g\rho_0\, z$. $\eta(p(z), p(Z))$ measures the departure of the thickness between isobaric surfaces near depths Z and z from its nominal value of $(Z - z)$, due to variations in water density from ρ_0. $\eta(p(z),p(Z))$ is defined as

1. CSIRO Marine and Atmospheric Research, GPO Box 1538, Hobart, Tasmania 7001, Australia
2. Corresponding author. ***email: stootrish@gmail.com***

$$\eta(p(z), p(Z)) = \int_{p(Z)}^{p(z)} SVA(T(z'), S(z'), p(z'))dp(z')/g$$

where Specific Volume Anomaly (SVA) is the difference between the inverse of water density at temperature T, salinity S and pressure p, and the same quantity at the standard temperature of 0°C and salinity 35 psu. Q is $(1/\rho_0 g)$ times the integral of $\eta(z,Z)$ with pressure from $p(Z)$ to the surface, or:

$$Q(Z) = \int_{p(Z)}^{0} \left\{ \int_{p(Z)}^{p(z)} \left\{ SVA(T(z'), S(z'), p(z'))dp(z')/g \right\} \right\} dp(z)/(\rho_0 g).$$

To Boussinesq approximation, this may be regarded as the depth integral of steric height with units of m^2. Exchanging orders of integration, and using the hydrostatic relation, yields:

$$Q(Z) = \int_{p(Z)}^{0} z(p)SVA(T(p), S(p), p)dp/g. \tag{1}$$

As used below, the symbol Q is divided by g compared to Sverdrup's use of this symbol, to preserve the identity of Q to the Depth-Integrated Steric Height (DISH) of G89. From the maps of Q in this paper, the geostrophic flow in the top Z meters between two deep-ocean points, relative to an assumed depth of no motion at depth Z, can be obtained as (g/f) times the Q difference between the points. Here f is the Coriolis parameter. One final, useful identity is that g times Q is essentially identical to the depth-integrated potential energy above depth Z (Gill, 1982).

G89 found quite good agreement over most of the global ocean between the wind-driven estimate Q_W from the G89 model, and the Q calculated from (1) using the Levitus (1982) estimates of annual mean temperature and salinity. Two key assumptions in G89 were that the Sverdrup relation (Sverdrup, 1947) is valid throughout the ocean interior, and that horizontal flow is zero everywhere along some constant "depth of no motion," Z. Sverdrup (1947) used the second assumption in demonstrating the usefulness of the first, in the tropical east Pacific.

However, observed Q along five oceanic eastern boundaries—western Australasia; western Sumatra–Thailand-Myanmar; west India; west Madagascar; and the east Atlantic—differed quite strongly from values found along the southeastern Pacific coast. G89's wind-driven model also gave useful estimates of these differences. (The observed value of Q along the west coast of New Zealand, relative to South America, was not well-simulated.) This agreement did not depend on the Sverdrup relation, but on other assumptions in G89. These assumptions are discussed in detail below, in Section 2.

This paper is concerned with comparing maps of Q_w from the G89 model with those of Q from (1), using more recent wind stress and hydrographic observations. The aim is to

locate regions where the G89 assumptions may seriously fail—apart from those already identified in G89, namely the Antarctic Circumpolar Current (ACC) and the Agulhas Retroflection.

Section 3 displays global maps of annual mean Q from the annual mean hydrographic data of Levitus (1982; from a version of the CARS climatology (Dunn and Ridgway 2002), that excluded Argo data; and also from the time-average of hydrographic data from Argo floats. The different methodologies used to obtain them are described here.

Section 4 shows maps of Q_w from two representative wind stress products, namely (a) Hellerman and Rosenstein (1983) (referred to below as HR wind stresses), which used ship wind speed observations with drag coefficients due to Bunker (1976) and (b) microwave reflectance measurements from the ERS satellite scatterometer (referred to below as ERS wind stresses). Bentamy *et al.*(2003) used direct wind vector measurements from ocean moorings, in conjunction with the drag coefficients of Smith (1988) to calibrate the reflectances. Wind stress products based on near-global satellite observations of microwave reflectance, such as from ERS and Quikscat, have been shown to capture some small-scale features of the real wind stress that were previously unknown; e.g., Kessler *et al.,* 2003; Xie *et al.,* 2001; and O'Neill *et al.,*2003. In the Southern Hemisphere, the direct spatial sampling underlying ERS winds is greatly superior to that for HR winds, and also to that for reanalysis winds. For brevity, Q_w maps from reanalysis winds are not used here because the lack of calibration against direct wind stress observations make them unreliable in the Antarctic. Section 4 also discusses spatial differences between the two Q_w maps; and differences in pattern amplitudes, resulting from the different choices of drag coefficient.

Section 5 considers model performance in more detail than in G89, in simulating observed values of Q along eastern oceanic boundaries—and also along western boundaries, at locations where G89 theory predicts that the Q difference across the western boundary current should be zero (or estimable from adjacent eastern boundary Q values, near the meridional tip of a land mass).

Section 6 examines open-ocean pattern differences between Q and Q_w, north of the "ACC boundary" (defined here as the circumpolar zero contour of Q). Sverdrup theory fails completely south of this boundary (e.g. Johnson and Bryden 1989; Wells and de Cuevas 1995; Hughes *et al.,* 1998), but it is at least useful in most places north of it. Departures from Sverdrup balance are much greater and more widespread than in the Northern Hemisphere, in a band about 1000-km wide north of the ACC boundary. Furthermore, while (nearly) every "meridional tip jet" seen in maps of Q_w has an equivalent in maps of Q, the path of the former is strictly zonal west of the tip, while the latter tend to veer toward the direction of ambient Sverdrup flow—not just in the first thousand kilometers north of the ACC boundary, but at other latitudes.

Section 7 describes how recent discoveries concerning the dynamics of the strongest parts of the ACC, near the ACC boundary, may provide a model for exploring the

dynamics of weaker departures from Sverdrup balance discussed in Section 6. The findings of this paper are summarized in Section 8.

2. Mathematical basis of the G89 model

Godfrey, 1989 assumed that:

(A) all continental shelf edges are vertical above the chosen depth of no motion, so Q is well-defined throughout the model ocean;

(B) onshore depth-integrated Ekman and geostrophic flows along eastern boundaries are equal and opposite, leading to:

$$g\frac{\partial Q}{\partial l} = \frac{\tau^{(l)}}{\rho} \tag{2}$$

where l is longshore distance, g is gravity, ρ is mean density and $\tau^{(l)}$ is longshore wind stress;

(C) the basin-wide meridional transport $T(y)$ through latitude y is the sum of zonally integrated meridional Ekman and geostrophic flows across an ocean basin, so that:

$$g(Q(x_E(y), y) - Q(x_W(y), y)) = \int_{x_E(y)}^{x_W(y)} \frac{\tau^{(x)}}{\rho}\, dx + f(y)T(y) \tag{3}$$

with $x_E(y)$, $x_W(y)$ the bounding longitudes of the basin and $f(y)$ the Coriolis parameter. It is thus assumed that the alongshore component of western boundary flow is geostrophically balanced. However, the smaller longshore gradients of Q_w along western boundaries are not necessarily geostrophically balanced.

(D) On time average, no mass transport passes vertically through the depth of no motion, so that a volume transport streamfunction $\psi(x,y)$ is assumed to be valid above the chosen depth of no motion. Because the Bering Strait is assumed to be closed, the streamfunction is zero along all coastlines, except those of the three islands retained in G89. (Note that this assumption of no transport through the depth of no motion is equivalent to assuming that all density-driven, deep northward flow from the Antarctic returns south below the chosen depth of no motion—possibly useful in the Pacific and Indian Ocean, but certainly violated in the Atlantic.)

(E) Q was assumed to be continuous at points where eastern and western boundaries meet. Hence, round-island transports can be estimated by an "Island Rule." This permits Q to be estimated via (2) and (3) along the island's west coast. For example, the streamfunction for New Zealand is:

$$\psi_{NZ} = -\oint_{ADCBA} \frac{\tau^{(l)}}{\rho}\, dl/(f_{NZN} - f_{NZS}) \tag{4}$$

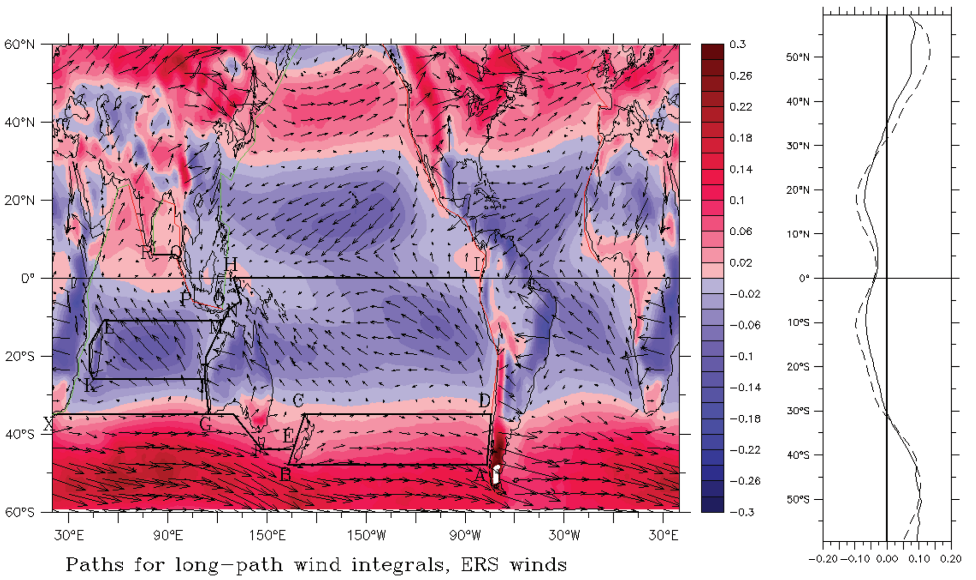

Figure 1. (a) The black lines and letters show integration paths for longpath wind stress integrals, for evaluating Q at the southeast corners of six ocean basins described in the text and the table, relative to the point A at 48°S on the South American coast. Colors show annual mean ERS zonal wind stress, while the vectors show longterm mean ERS wind stresses. Red, green lines show the G89 approximation to eastern, western boundary locations. (b) The full/dashed lines show ERS/HR zonal wind stresses, along 30°W.

where f_{NZN}, f_{NZS} are Coriolis parameters at the northern and southern tips of New Zealand. ADCBA is the closed path seen in Figure 1. (The sign of the Island Rule is reversed compared to G89, to conform with the usual definition of the streamfunction via ($\psi_x = V$, $\psi_y = -U$).) Wajsowicz (1993a) extended this rule for situations where the channel between an island and its neighbor was too narrow for friction to be ignored, while Wajsowicz (1993b; 1996) extended it further (via an electric circuit analogy) to groups of islands, such as Indonesia. Pedlosky *et al.* (1997) extended the original Island Rule in a number of ways, including use of numerical models and laboratory experiments to test the usefulness of the rule over a range of nonlinear and frictional conditions.

The transport between Australasia (Australia and New Guinea, with Torres and Bass Straits closed) and South America was inadvertently calculated in G89 as if New Zealand were absent. The correct, two-island rule is:

$$\psi_{Aust} = -\left\{(f_{AustS} - f_{NZS})\psi_{NZ} + \oint_{AIHGFEBA} \frac{\tau^{(l)}}{\rho}\, dl\right\} / (f_{AustN} - f_{AustS}). \qquad (5)$$

From the above rules, once the circulations around the three islands of New Zealand, Australasia and Madagascar have been calculated from the Island Rule, Q_w can be calculated at each of the southeast landmass tips B,F,O,R,K,X of Figure 1 relative to Q_w at A (taken arbitrarily to be zero) as detailed in the Appendix, along one or more of the paths shown in black in Figure 1. The table gives the numerical results for ERS and HR wind stresses. Note that we have been unable to convert the original Fortran code used for these calculations to more convenient software, so no attempt has been made to increase the number of islands represented, or to alter the various simplifications in the original choice of coastlines.

(F) Finally, the Sverdrup relation was assumed valid throughout the ocean interior, to within one grid interval of the western boundary. Thus ocean interior Q_w is obtained from

$$gQ_W(x, y) = gQ_W(x_E(y), y) + \frac{f^2}{\beta}\int_{x_E(y)}^{x} curl\left(\frac{\tau}{\rho_0 f}\right)dx. \tag{6}$$

The transport of the western boundary current is then the difference between the total flow between that boundary and the nearest eastern ocean boundary to its east, obtained from assumptions (C)–(E), and the net Sverdrup interior flow at that latitude.

Useful qualitative information about the wind integrals of the Appendix, and hence about coastal Q_w values throughout the world, can be obtained simply by inspection of the paths and annual mean ERS wind stress vectors shown in Figure 1. For example, the last equation from the Appendix states:

$$g^*(Q_W(X) - Q_W(A)) = -\int_{XGHIA}\frac{\tau^{(l)}}{\rho}\,dl - f(36°S)^*\psi_{Aust} + f(0°S)^*\psi_{Aust} \tag{7}$$

i.e. Q_w at the southern tip of South Africa at 36°S relative to that at A (at 48°S, off Chile) may be calculated as the sum of the long-path wind stress integral $\int_{XG}\frac{\tau^{(l)}}{\rho}\,dl$ along the path XG of Figure 1, and the integral $\int_{GHIA}\frac{\tau^{(l)}}{\rho}\,d$ along the path GIHA, plus a term $(f(36°\mathrm{S}) - f(0°S))^*\psi_{Aust}/g$, involving the round-Australia circulation ψ_{Aust}. Inspection of the stress vectors in Figure 1 suggest that the two path integrals will be of opposite sign, and of similar magnitude. This is confirmed by the fact that, for ERS winds, $-f(36°S)^*\psi_{Aust}/g$ is $-111.9\ \mathrm{m}^2$—close to the more accurate value (see Table 1) of $[Q_w(X) - Q_w(A)]$ from (7) of $-105.6\ \mathrm{m}^2$, because the two integrals almost cancel. Because the Island Rule has been used, the same numerical answer for $Q_w(X) - Q_w(A)$ can be obtained from similar formulae, following paths from A to X via the north or south tip of New Zealand and via southern Tasmania.

Table 1. Relationships on circulations around islands, T, and on Q at southeast corners of basins.

Quantity	HR	ERS
ψ_{NZ}	−29.5 Sv	−26.5 Sv
Ψ_{Aust}	−17.0 Sv	−13.1 Sv
$\Psi_{Madag} - \Psi_{Aust}$	−4.0 Sv	−3.5 Sv
Q'(B)	219.6 m^2	196.9 m^2
Q'(F)	83.7 m^2	52.8 m^2
Q'(O)	43.4 m^2	25.5 m^2
Q'(R)	40.1 m^2	24.4 m^2
Q'(K)	136.7 m^2	104.6 m^2
Q'(G)	66.5 m^2	42.7 m^2
Q'(X)	−129.6 m^2	−105.6 m^2

3. Maps of Q from hydrographic observations

Figure 2a shows annual mean Q relative to 1500 db, using (1) and the gridded time-average of all hydrographic data given by Levitus (1982). For brevity, the only choice of the depth of no motion, Z, shown in this paper is 1500 db; sensitivity to other choices was adequately explored in G89. SVA is obtained from Levitus (1982) data on temperature $T(p)$ and salinity $S(p)$ on a $1° \times 1°$ grid; these are obtained as weighted averages of data from all hydrographic casts within about 700 km of the point. The same procedure was followed using the later data set of Levitus (1998); the results were sufficiently similar to Figure 2a that they are not shown here. The range of Figure 2a is −1000 m^2 to +1000 m^2, with a contour interval of 40 m^2—slightly smaller than in G89. This same range and interval is used throughout Figures 2 and 3.

Q relative to 1500 db has also been obtained from a version of the CARS data set (Ridgway *et al.,* 2002) using ship-based hydrographic data only, i.e. Argo data were omitted from it (Fig. 2b). The CARS temperature and salinity data set consists of all available hydrographic cast data up to 1999, in the domain shown. These data were mapped onto a 0.5° global grid on standard depth levels, using "loess," a locally-weighted least-squares quadratic smoother, which permits smoothing to be adjusted based on local data density. This results in higher resolution than in Levitus (1982) and Levitus *et al.* (1998) in most places. Annual and semiannual harmonics were fitted at the same time so that the mean field is free of seasonal signals. The mapping scheme also restricts "leakage" of data influence across narrow land features such as the Indonesian islands. Q was calculated directly from the gridded profiles of annual mean temperature and salinity. An offset of 950 m^2 was subtracted to bring the values to zero at the point A of Figure 1, for closer comparison with the wind-generated Q fields.

Figure 2c is similar to Figure 2b, from Argo data only; the data set of Figures 2c is completely independent of those from Figures 2a,b. All available quality-controlled hydrographic data were downloaded from the Argo global data centers, excluding floats known to have pressure-sensor errors. Pressure drift adjustment using the surface pressure

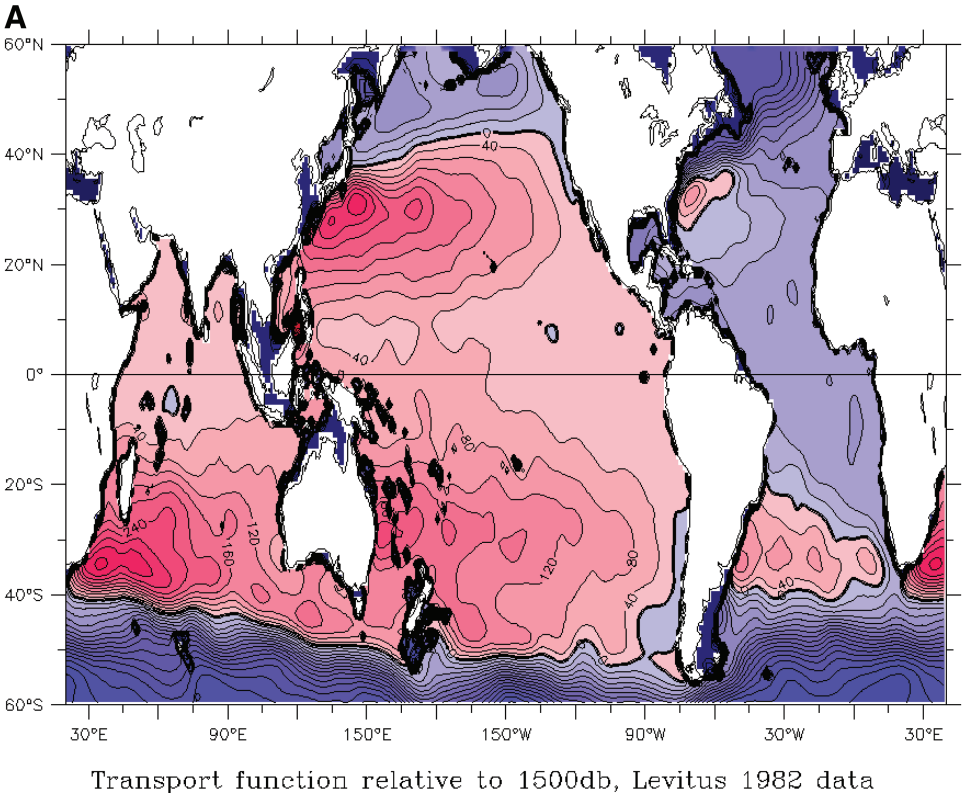

Figure 2. (a) Colors indicate values of long-term mean $Q(1500)$ evaluated from the Levitus (1982) climatology of temperature and salinity, relative to zero at the East Pacific boundary at 48°S. In all panels of Figures 2 and 3, the dark contour is zero, and the contour interval is 40 m^2.

value was applied for all positive-drifting APEX floats (Barker *et al.,* in prep). Profiles were then interpolated to a set of 67 standard depth levels, spanning 0 to 2000 m. Points strongly deviating from the CARS seasonal climatology were rejected. This final quality check removed less than 2% of the data. The "loess" processing in Figure 2c is identical to that of Figure 2b. Figure 2c has a more noisy appearance than Figure 2b, because the data density is greater and more spatially even in Argo than in the CARS data set, so sampling is performed over shorter distances from the target point, especially in the Southern Hemisphere.

Comparison of Figures 2a,b and c reveals many similarities on basin scales or larger. The well-known subtropical and subpolar gyres are clearly evident in all three pictures (except outside the domain of CARS data), with similar relative strengths. The differences between mean values of Q along the different eastern boundaries are also clearly evident in Figures 2a–c, and similar in all. For example the values are -20 to 40 m^2 on the Pacific eastern boundary, 50 to 120 m^2 along the west coast of Australasia and -120 m^2 to

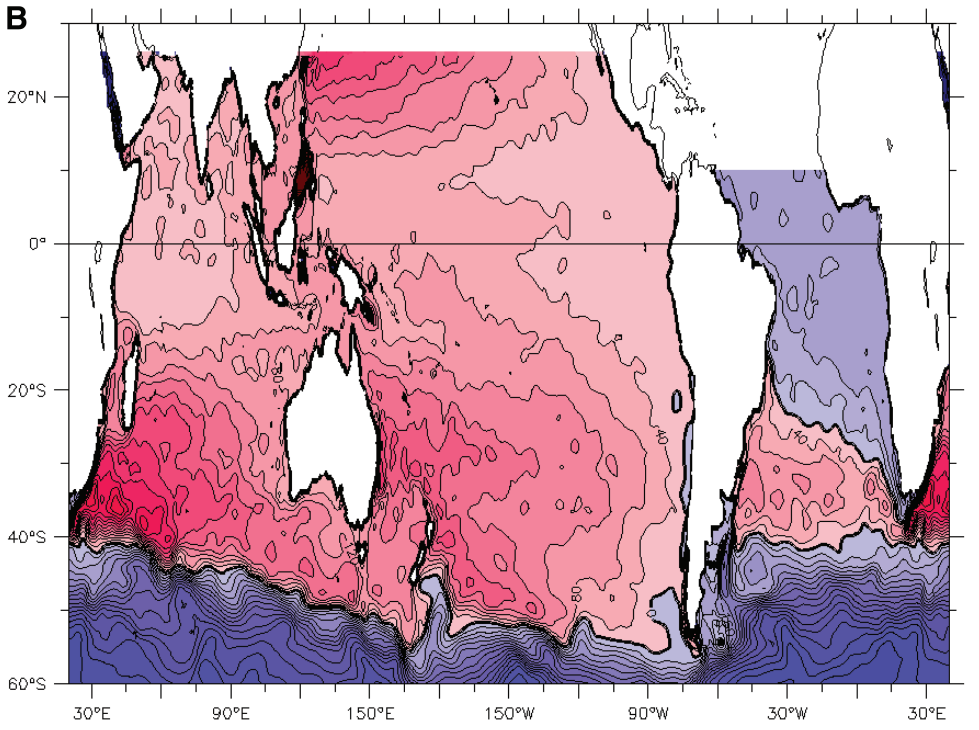

Figure 2. (continued) (b) A Q map prepared as described in the text, from all traditional hydrographic casts available from international and Australian data centers for CARS (Ridgway *et al.,* 2002). Note that CARS data do not extend beyond 30°N.

-80 m^2 along the Atlantic eastern boundary. In particular, the lower values of Q along the eastern Atlantic boundary, relative to any of the other basins, is so great that Q is seen to be negative (relative to zero in the southeast Pacific) in the entire Atlantic, apart from the cores of the Gulf Stream and Brazil Current gyres. North of the ACC, the only other region of negative Q is the polar and subpolar north Pacific.

All three figures show long "tongues" of high Q, stretching east in each basin along and to the north of the ACC boundary; these turn out not to be well-simulated by G89. A number of other, relatively small features, can also be seen in all three figures. For example, a zonally-narrow minimum in Q is seen along the South American coast centered at about 30°S; an intense warm-core eddy remains locked about 1000 km west of South Africa, near 32°S; and a westflowing jet leaving the southwest corner of Australia (Cape Leeuwin) moves northward with the broader geostrophic flow, within a few hundred kilometers of leaving their points of origin. As will be seen, all these features have no clear analogs in the maps of Q_W; they are the focus of this paper.

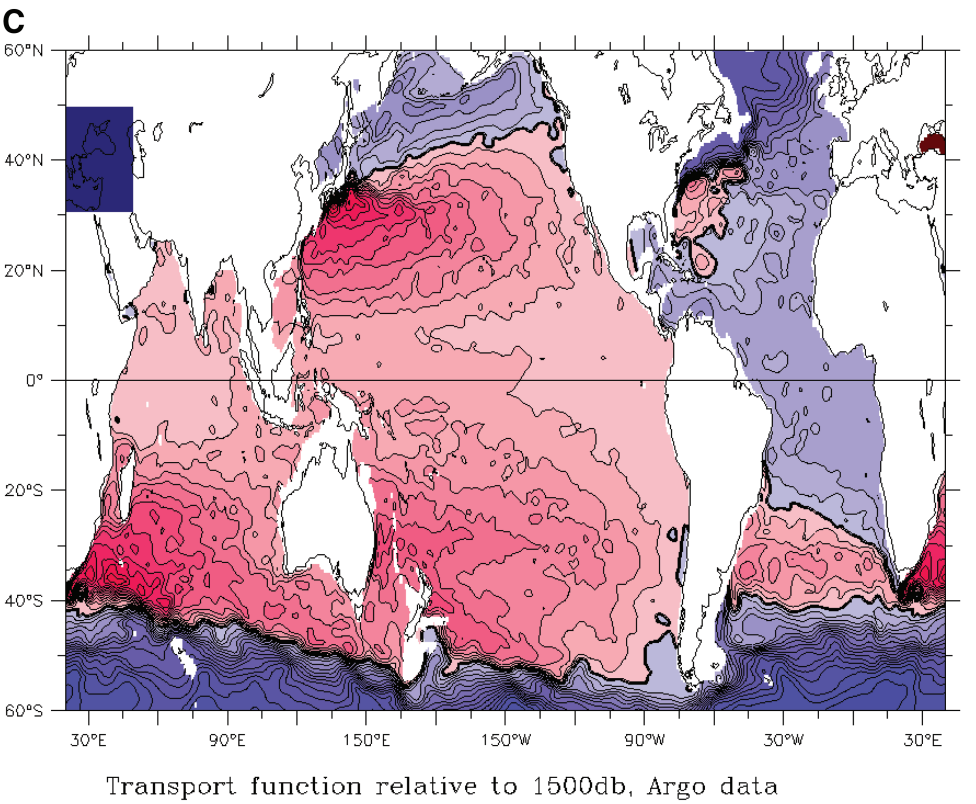

Figure 2. (continued) (c) A Q map prepared as described in the text, from Argo hydrographic data obtained since 1999.

The data of Figure 2a were all obtained before 1982, while that for Figure 2c was obtained from Argo floats, i.e. since 1999. The difference map between them (not shown) reveals a small increase in Q nearly everywhere north of the ACC. This increase is very much accentuated along the axis of the ACC and in the Gulf Stream Outflow, where it is over 200 m^2 in places. Q in the far northwest Atlantic is also markedly increased, as can clearly be seen in the lighter blue color of Figure 2c compared to Figure 2a in this region. However, this time-dependent difference is not considered further in this paper.

4. Maps of Q from wind products

Figures 3a–b show global maps of long-term mean Q_w, evaluated from wind products according to the procedures of G89 (apart from the use of (5) to evaluate transport around Australasia) from HR, ERS winds respectively.

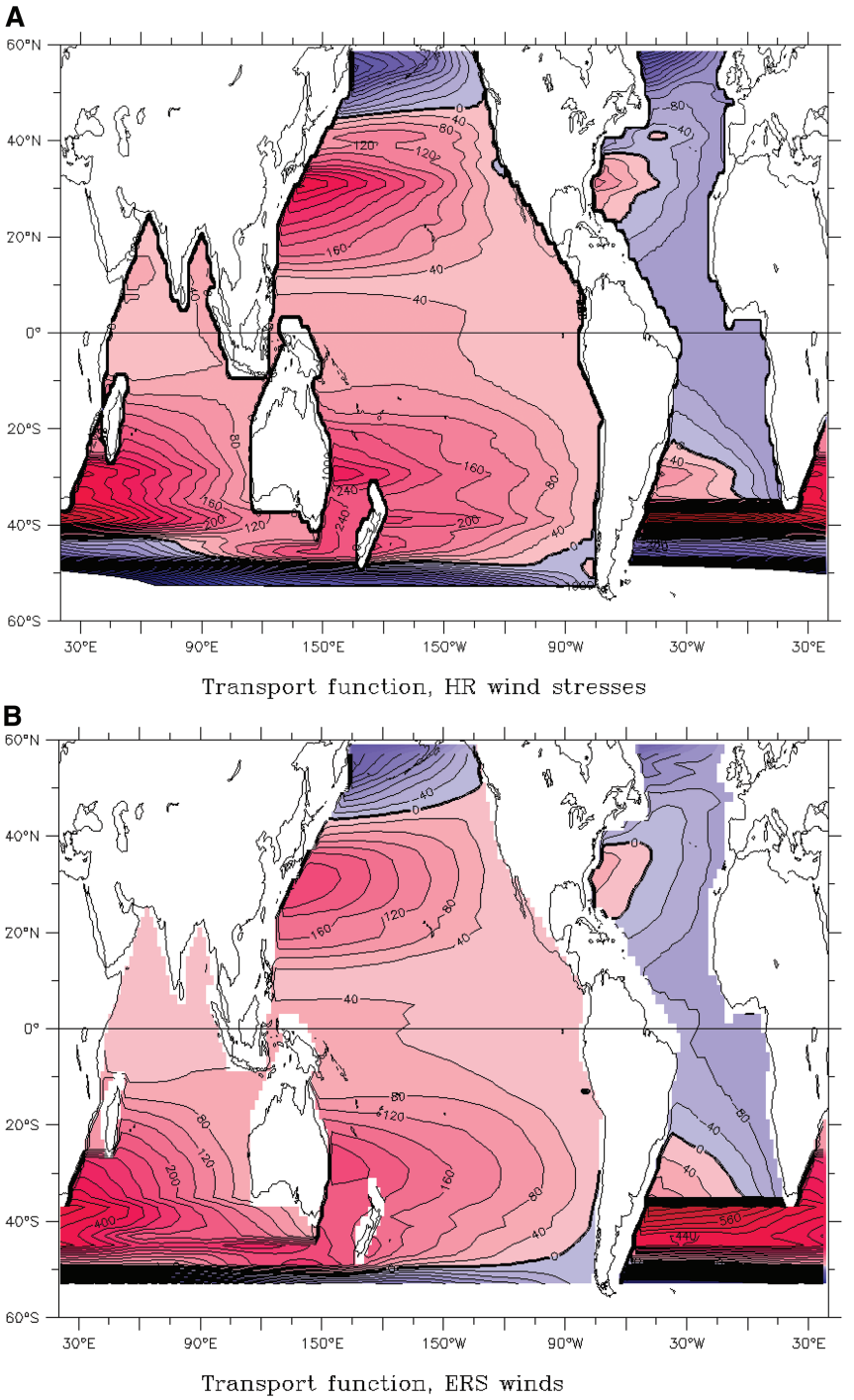

Figure 3. (a) As for Figure 2a, but for Q_w calculated from the HR global annual mean wind stress product. (b) As for Figure 2a, but for Q_w calculated from the ERS global annual mean wind stress product.

a. Similarities and differences among wind products of spatial Q_w patterns

The wind products of Figure 3 both reproduce the major gyres seen in Figure 2. One point of agreement that is evident in the original G89 maps, but was not explicitly mentioned there, is that the southwest-northeast slope of the boundary between the subtropical and subpolar gyres seen in Figure 2 is also well simulated, in the North Pacific and Atlantic. This occurs because the real winds are used, rather than the zonal-mean mean winds often used in idealized studies. Because the Q_W field (with real winds) matches observed Q quite well, the well-known nonlinear intensification of Q gradients at the confluence of the western boundary currents of the polar and subpolar gyres, visible in the North Pacific and Atlantic in Figure 2 compared to Figure 3, appear as fairly local phenomena on the global scale. Figure 3 also qualitatively reproduces the interbasin differences in Q along eastern boundaries in Figure 2.

However, there are quite large spatial pattern differences between the wind maps. This is not surprising. HR wind stresses were obtained by digitizing "wind roses" from mariners' wind atlases. The data for HR winds are therefore confined to shipping lanes, resulting in inadequate data in the Southern Hemisphere. By contrast ERS winds were obtained from abundant, spatially-uniform microwave ocean roughness observations from satellites, calibrated against wind vector observations from moorings. It is therefore to be expected that the ERS winds will provide a much more reliable spatial pattern than HR winds do. Figures 3b indeed shows smoother, more "believable" gyre structures in the Southern Pacific Ocean than those from Figures 3a.

b. Amplitude of spatial Q_w patterns

Comparison of Figure 3a, b shows a clear tendency for the amplitude of Q_w patterns to be larger with HR winds than with ERS, throughout the globe. The most likely reason is that this is due to different choices of drag coefficients in the two stress products. HR used those of Bunker (1976). Bentamy *et al.*(2003) calibrated the ERS measurements of microwave scattering against observed wind velocities at mooring sites, from which bulk stress estimates were obtained using the drag coefficients of Smith (1988). Thus—although the quantity measured (microwave scattering) should be a measure of wind stress, regardless of wind speed—drag coefficients enter the estimation through this calibration process.

The annual mean wind stresses used to generate Figure 3 are dominated by contributions from moderate to strong winds; the bulk Richardson stability parameter Ri_b for the atmospheric boundary layer (e.g. Fairall *et al.,* 2003) is generally quite small at these wind speeds, so the drag coefficient is dominated by its value at neutral stability. Figure 4 shows the neutral bulk transfer coefficient from Bunker (1976) and from Smith (1988) as a function of wind speed; also that of Fairall *et al.* (2003). The neutral drag coefficient of Bunker (1976) is about 30% larger than that of Smith (1988) at all wind speeds, broadly consistent with the higher amplitudes of Q_w variations in Figure 3a compared to Figure 3b. Fairall *et al.*'s neutral drag coefficient is also shown in Figure 4. It is intermediate between

those of Smith and Bunker, matching that of Smith (1988) up to speeds of 12 m s^{-1}, but they become steadily larger than Smith's at higher speeds.

The Fairall *et al.* drag coefficients are the fruit of a very extensive collection of direct eddy-flux measurements of drag in environments ranging from the Pacific Warm Pool to the Arctic, and the authors claim that stresses estimated from their new bulk algorithm matches their eddy correlation measurements to 10% or better over the entire range of the latter. Thus a wind product based on these drag coefficients and ERS winds would be highly desirable for oceanographic research purposes.

5. Interbasin *Q* differences along ocean boundaries

a. Tests of interbasin Q differences along eastern boundaries

Figure 5 shows latitude-by-latitude comparison of the model with Argo data for each eastern boundary (only the Argo data has been used since it is more likely to resolve coastal features than the heavily smoothed data of Levitus (1982) and Levitus *et al.* (1998), especially in the presence of intense longshore flows like that along the west South African coast, Fig. 2c). Observations and both wind-generated *Q* estimates agree quite closely (as in G89, New Zealand is the exception), but the *Q* observations show systematic departures with longshore length scales of over 1000 km in many cases. For example, the elongated region of relatively low *Q* centered near 30°S along the South American coast extends for 1500 km. While the possibility that this is due to local inadequacies in Argo data cannot be discounted, as mentioned in Section 3, this feature is visible in all panels of Figure 2. Other examples can be seen along other coastlines. No attempt is made here to diagnose the physics (or data limitations) behind these departures from the simple G89 physics. However, they are not negligible: for example, *Q* rises by about 30 m^2 from 25°S to 20°S along the South American shelf edge. If this were balanced geostrophically, an onshore flow of about 6 Sv would be produced that appears not to be balanced by offshore Ekman transport.

The eastern Indian Ocean boundary opposite Australasia shows quite strong departures from G89, as discussed in Godfrey and Masumoto (1996). One reason is that the coastline from Tasmania northward has a section of western boundary on the western end of the Great Australian Bight. This coastline feature is replaced with a zonal coastline in Figure 3. Substantial northward Sverdrup transport impinges on Australia's south coast, generating the "Flinders Current" (Middleton and Cirano, 2002). Secondly, the strong Leeuwin Current along the west coast of Western Australia—although balanced by a roughly equal and opposite Leeuwin Undercurrent—certainly complicates the applicability of (2) along this coast. Eq. (2) appears to hold roughly as well along the Indonesia-Myanmar, west Indian and Madagascar coasts as along the East Pacific coasts. As in G89, Figure 5 does not capture the behavior of *Q* along the New Zealand west coast. The New Zealand coast has broad, shallow outliers in the Campbell Plateau to its south, Chatham Rise to the east and Norfolk Rise to the northwest (white areas in Fig. 2 are less than 1500 m deep). These

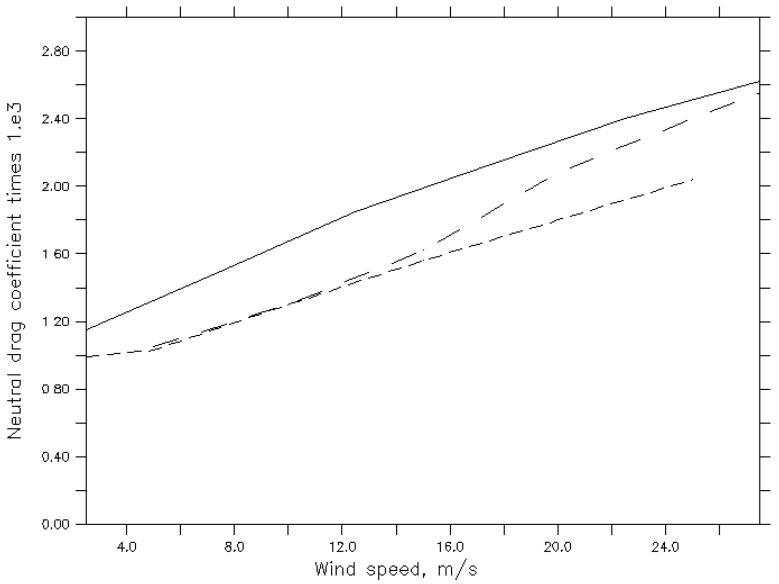

Figure 4. Neutral drag coefficients from Bunker (1975) (full line); Smith (1988) (short dashed line); and Fairall *et al.* (2003) (long dashed line).

shallow regions are all likely to affect the applicability of G89. Also, Hill *et al.* (2008) have shown that on timescales of a few years, barotropic Rossby waves in mid-Pacific advect Q patterns around New Zealand; this non-G89 effect may also apply on long-term mean.

b. Q along the inner edges of western boundaries

The red and full black lines in Figure 6a shows $Q_W(y)$, i.e. Q along the inshore edge of the western boundary according to the G89 model from the HR/ERS winds respectively, for the western Pacific.

Q is effectively discontinuous across the WBC, so at most latitudes the smoothed observational data in Figures 2a–c cannot be compared reliably with G89. However, at predicted stagnation points the G89 western boundary current $T_{WBC}(y)$ is zero, so inshore and offshore Q should be the same. They will also be the same on the equator, where f is zero.

The red/blue asterisks in Figure 6a show observed values of Q just offshore from the western boundary at these locations, from the climatologies of Levitus (1982) and Argo, respectively. Agreement is surprisingly good, given the known nonlinear nature of western boundary currents. The two data points in the North Pacific mark the northern and southern ends of the Kuroshio; $g\rho_0$ times the Q difference between them may be thought of as the depth-integrated "pressure head" driving the Kuroshio against nonlinear frictional effects. Similarly, $g\rho_0$ times the Q difference from 18°S to 44°S is the depth integrated pressure head along the East Australian Current. The data points at 44°S have been obtained from

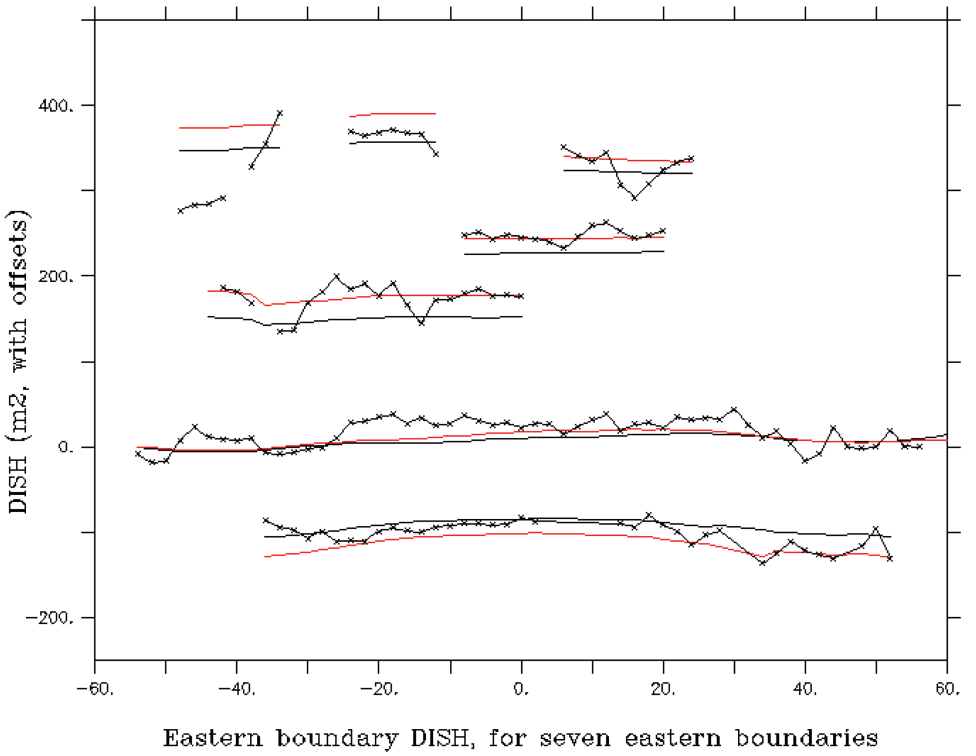

Figure 5. Comparison of observed and wind-calculated Q along eastern boundaries. Seven groups of three lines are displayed. Where necessary, each line triplet has been displaced vertically by an arbitrary amount to prevent overlap. In each group, the red and black curves show Q according to the G89 model as a function of latitude, along one of the model's seven eastern boundaries, using HR and ERS winds, respectively. The line with crosses is from the Argo Q data set of Figure 2c, closest to the eastern coast. From bottom to top, the coasts are: east Atlantic; east Pacific; west Australasian coast; Indonesia-Bangla Desh coast; and (along the top row, from left to right) New Zealand west coast, Madagascar west coast, and eastern Arabian Sea.

just west of Southern Tasmania. The smaller pressure head along the EAC relative to the Kuroshio is due to the fact that the Island Rule raises Q at 44°S, compared to the value it would have if the Indonesian gap were closed. The departure of observed Q from G89 at 42°N in Figure 6a may be a nonlinear phenomenon due to this point lying within the Kuroshio-Oyashio convergence zone.

The full lines in Figure 6b are the same as Figure 6a, for the inner edge of the western Atlantic. In this case observed Q agrees with the model on the equator; departures of model from observation are roughly linear with Coriolis parameter. The magnitudes of these model/observation differences are consistent with a depth-integrated net northward flow T_{NADW} of order 16 Sv above the depth of no motion to supply the sinking of North Atlantic Deep Water, as suggested by Gordon (1986). The resulting estimates of western boundary

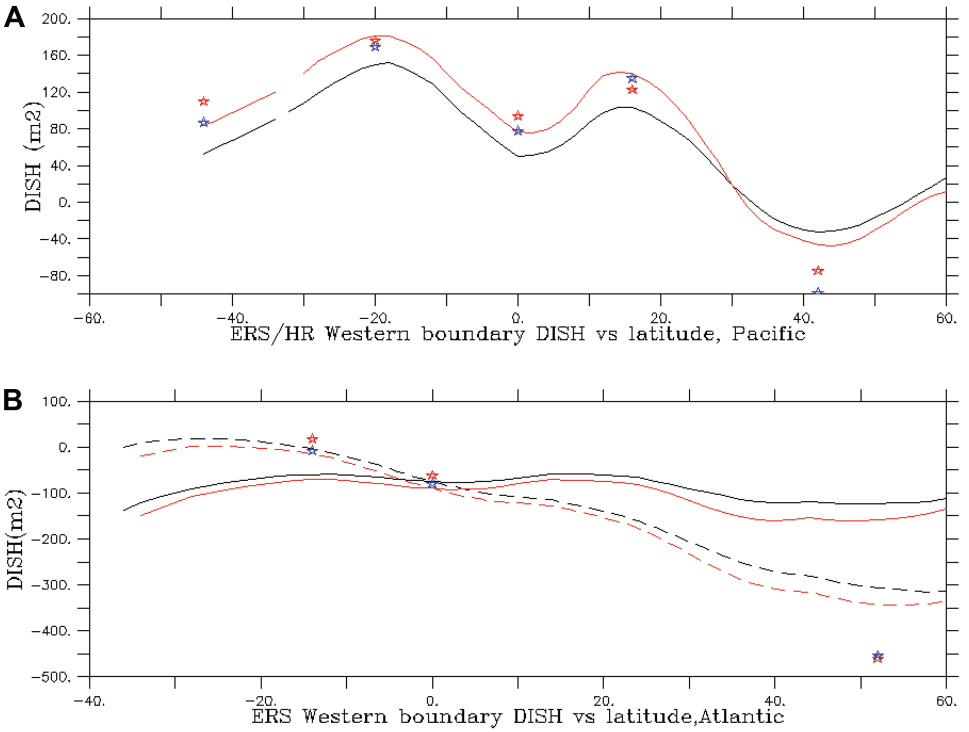

Figure 6. (a) The full black and red lines show Q_W as a function of latitude along the inner edge of the Pacific western boundary, for ERS and HR winds respectively. The red and blue asterisks show observed values of Q a short distance offshore, from the data of Figures 2a and 2c respectively. The data at 44°S were taken from just west of Tasmania's southern tip. (b) As for Figure 6a, for the west Atlantic coast, but with addition of dashed lines indicating the addition of a term $-f(y)*T_{NADW}/g$ to the full line of the same color; T_{NADW} is a (non-Sverdrup) upper layer transport of 16 Sv (Gordon, 1986). The graph is truncated at 40°S, since the Sverdrup relation does not apply farther south than that (e.g. Wells and de Cuevas, 1995).

Q are obtained by subtracting a term $f(y)T_{NADW}/g$ from the data plotted in the full black and red lines. As in the North Pacific, the departure of the model from observations at 50°N may reflect a nonlinear phenomenon, this time associated with the Gulf Stream–Labrador Current confluence. Further points could be added to Figures like Figures 6a,b wherever data from mooring arrays are available, by allowing for the depth-integrated steric height difference between a point offshore and the coast, allowing at each depth for the Coriolis force acting on the measured transport per unit depth. However, no attempt to do this is made here.

6. Open-ocean departures of observed Q from theoretical Q_W

Comparison of Figures 2 and 3 show massive differences south of the ACC boundary (defined earlier as the circumpolar zero contour of Q in Fig. 2), as expected from the fact

that the dynamics of the ACC are now known to be fundamentally different from Sverdrup dynamics.

Large positive wind curls occur between 36°S and 44°S, and at all longitudes between Australia and South America. When these are integrated westward from the Australian (or south New Zealand) coast, as done in Figure 3, very high Q_W values are predicted in the west Indian and Atlantic Oceans. The (spurious) intense, westflowing "Agulhas Jet" of Figure 3 separates this band of very high Q_W from the much lower values found in the south Atlantic.

The observations (Fig. 2) show that the Malvinas Current moves north up the Patagonian shelf to 38°S, and the remainder of the ACC moves eastward. Hughes *et al.* (1998) showed that the direction of propagation of time-dependent anomalies in surface temperature and sea level was westward nearly everywhere north of the ACC boundary, and eastward nearly everywhere south of it. This suggests that net vertically averaged speeds are large enough in the ACC to reverse the westward speed associated with baroclinic Rossby waves. This eastward advection by the ACC stops the establishment of the Sverdrup relation by westward-propagating baroclinic Rossby waves (Anderson and Gill, 1975). Northward advection by the Malvinas Current (e.g. Vivier and Provost, 1999) and eastward advection by the ACC thus apparently sweeps away the warm, high Q_W waters of Figure 3, and replaces them with the cold waters that pass through Drake Passage, everywhere south of the ACC boundary. These phenomena will be explored further in a later paper, using expanded versions of Figure 2c in each ocean basin south of about 20°S.

This section is concerned with describing large-scale departures of observed Q from theoretical Q_W found north of the ACC boundary, where Sverdrup dynamics are at least qualitatively useful. Near the ACC boundary, the observed large-scale features of Q in Figure 2 are simpler than the Q_W of Figure 3, so this description is best done by comparing the individual panels of Figures 2 and 3. The concern here is with features with quite long lengthscales, so these figures are adequate for the purpose.

Inspection of the panels of Figure 2 show that in each of the three ocean basins, a "tongue" of high Q about 1000 km wide in the meridional direction is to first approximation aligned parallel to the ACC boundary, and just north of it, extending the subtropical gyre eastward relative to Figure 3. Each tongue emanates from one of the three points where the western boundary currents go seaward.

In the South Atlantic, the "tongue" of high Q emanates from the Brazil-Malvinas Convergence, near 38°S (e.g. Vivier and Provost, 1999). The South Atlantic Current (Stramma and Peterson, 1990) flows strongly eastward right across the Atlantic near this latitude, as can be seen in Figure 2. Q contours are seen to be "compressed" strongly into the eastern Atlantic, north of 36°S, in Figure 2 compared to Figure 3. Hughes *et al.* (1998) show that time-dependent anomalies in SST and sea level move eastward in the SAC as well as in the ACC, reversing the sign expected from Rossby waves. Thus this non-Sverdrupian eastward compression of Q contours in Figure 2 relative to Figure 3 may be due to eastward advection of Q anomalies by the SAC (which may extend deeper than

1500 m, due to inclusion of some of the Malvinas Current), just as the failure of the Sverdrup relation everywhere further south may be due to strong eastward advection by the ACC.

In the Indian Ocean, part of the SAC is seen in Figure 2 circulating around the Agulhas Retroflection. The two continue east-southeastward, to rejoin the ACC. This conjunction of the SAC and Agulhas in the Agulhas retroflection is the point in the South Indian Ocean that corresponds to the BMC in the Atlantic. A wide region of non-Sverdrup behavior is seen east of it all the way to Campbell Plateau near 170°E, and for distances of order 1000-km north of the ACC boundary.

Finally, the Southland Current breaks from the ACC and moves northward along the east side of the Campbell Plateau and southern New Zealand, converging with the East Cape Current near 175°W, 42°S (Heath, 1975). The Southland Current appears to sink beneath the warmer East Cape Current, causing it to upwell. The combined Southland-East Cape Current loops back to the southeast, from the east end of Chatham Rise, to join the main ACC. The conjunction of the combined Southland-East Cape Current is the third point, southeast of which a tongue of high Q is seen in Figure 2 that is absent from Figure 3.

These tongues are similar to those east of the conjunction of the Gulf Stream and Labrador Currents in the North Atlantic, and that of the Kuroshio and Oyashio in the North Pacific. However, comparison of the northern and southern hemisphere versions of these phenomena shows that the departures of Q from Q_W seem to be much larger and more widespread in the Southern Ocean than in their northern hemisphere counterparts. This probably reflects the presence of the intense, non-Sverdrupian ACC just to their south.

Following these tongues eastward from their sources in each basin, flow is seen to leave the tongue northward, qualitatively as expected from the Sverdrup relation and the fact that these flows (at least near their western boundary origins) occur in regions of strong positive wind stress curl. Nevertheless, at least in the Atlantic and Pacific oceans, there are obvious large differences in the distributions of Q and Q_W north of the ACC boundary. In these two oceans, the form of these two tongues of high Q suggest that the deep, intense flow seen along the ACC boundary in Figure 2 is advecting depth-integrated relative vorticity $(g/f)\partial Q/\partial y$ for some thousands of kilometers eastward relative to what is expected from Sverdrup theory and Figure 3, as in western boundary currents; see also Kessler *et al.* (2003).

The situation in the Indian Ocean is more complex, because G89 theory predicts a very strong westward zonal jet west of southern Tasmania. Its volume transport is about 12 Sverdrups in Figure 3a; 16 Sv in Figure 3b. In all panels of Figure 2, there is no indication of a net westward flow starting from just south of Tasmania, with its associated meridional discontinuities in Q. This implies that the mean strength of the EAC near southern Tasmania is overestimated in Figure 3; though substantial interannual variations are known, e.g. Rintoul and Sokolov (2001) and Hill *et al.* (2008). Curiously, Rintoul and Sokolov find a net westward transport of 8 ± 13 Sv just south of Tasmania. However, their transport figures at this latitude were taken with a depth of no motion at the bottom, i.e.

near 2000–3000 m, and inspection of their Figure 2 shows that neutral density only has the sign of slope needed for westward flow below about 1000 m. Thus their result is compatible with our result of near-zero transport above 1500 m, relative to 1500 m.

This observational difference (relative to 1500 m) between Figures 2 and 3 is specific to this particular jet. All panels of Figure 2 show (noisy) equivalents of MTJs in other locations, such as that west of New Zealand's north tip or from either tip of Madagascar—and from islands not included in the G89 model topography such as New Caledonia, e.g. Qiu *et al.* (2009). Because the time-averaged difference in Q across the southern Tasmanian jet is near zero, (by coincidence or some presently unknown physical reason), there is no discontinuity in Q west of Tasmania in Figure 2. Thus a simple, well-defined "tongue" of high Q values is seen in the Indian Ocean in Figure 2, very like those in the South Atlantic and Pacific. In this sense, Figure 2 is simpler than Figure 3 in this region; the latter shows the Tasmanian MTJ strongly distorting the Q_W contours. The tongue in Figure 2 extends parallel to the ACC boundary, and ends at the western side of the South Tasman Rise.

A further feature of the observed Q in the Indian Ocean concerns the MTJ seen leaving Western Australia just south of Cape Leeuwin in Figures 2 and 3. This jet maintains the intensity of its flow for some thousands of kilometers downstream; but the MTJ in Figure 2 departs strongly from the Sverdup zonal path westward, seen in Figure 3. Instead the observed jet in Figure 2 flows northwestward or even northward, roughly parallel to ambient Sverdrup flow from Figure 3.

This tendency for such MTJ's to follow the local direction of the ambient Sverdrup flow is seen in several places. Thus a strictly zonal jet is seen in Figure 3b, west of Hawaii. Xie *et al.* (2001) noted the likely existence of such jets from satellite wind data, and showed that there was probably a coupled air-sea interaction mechanism permitting wind curls to extend farther west from the island than might be expected from island wind wakes. An MTJ can be seen in this location in Figure 2c, but its path lies west-southwest from Hawaii, near to the direction of ambient Sverdrup flow from Figure 3.

7. Notes on the dynamics of flows north of the ACC boundary

The above results suggest that there are large-scale, systematic departures of Q from simple Sverdrup theory, north of the ACC boundary. While not as dramatic as those south of it, they are still substantial. However, it is not obvious what mechanism replaces Sverdrup balance, wherever the depth-integrated meridional, geostrophic flow differs from the Sverdrup prediction of $(f/\beta)\mathrm{curl}(\tau/\rho f)$.

Luyten *et al.*(1983) showed how the characteristics for geostrophic flow in the upper layer of a two-layer system above an infinitely deep, inert "abyssal ocean" are determined by the sum of depth-averaged Sverdrup flow, and westward baroclinic Rossby wave velocity. If this is to be useful for understanding Q in Figure 2, there would need to be substantial deep flow beneath 1500 m. As noted earlier, the observations of Rintoul and Sokolov (2001) show that this situation does occur, in the southern Tasmanian MTJ. This

might also help explain features such as the northward flow of the Flinders "meridional tip jet" in Figure 2, after leaving southwestern West Australia.

An alternative explanation for the departures from Sverdrup balance discussed in Section 6 is that—as in the confluences of WBCs in the North Pacific and Atlantic—eddies form along those confluences, and are advected equatorward with the Sverdrup circulation. Nonlinear interactions between these eddies, or between eddies and features of the time-mean fields, may be sufficient to account for the departures from Sverdrup balance seen along the three southern hemisphere high-Q tongues.

Williams *et al.* (2007) consider the dynamics of flow in the ACC, especially along the "ACC boundary" defined earlier, from south of South Africa near 40°S, to the south end of the Campbell Plateau near (170°E, 56°S). They show that Eady growth rates are higher in a narrow band within a few baroclinic Rossby radii on either side of this line than elsewhere. Within this band, there are localized regions of particularly high growth rates, analogous to "storm tracks" in the atmospheric Jet Stream. They correspond to the west ends of the "braids" seen along the ACC boundary in Figures 2a,b. Baroclinically unstable eddies grow in these regions, as they move along the ACC boundary, accelerating the mean flow eastward. On entering a region of lower Eady growth rate, the eddies weaken and the current slows down. The baroclinic eddies also interact with the background baroclinic current to create barotropic eddies; these can transfer momentum, and vorticity, to the bottom. Here it may be dissipated by bottom pressure torques (e.g. Hughes, 2005).

It is possible that a weaker version of such eddy-driven dynamics may be operating to bring the flow back toward full Sverdrup balance, as the geostrophic flow moves northward away from the ACC boundary. As noted earlier, this appears to occur within about 1000 km of leaving the ACC boundary.

Eddies are often found off the west coast of Australia, with typical flow speeds 10 times faster than background annual mean flows. These eddies appear to interact with one another in nonlinear ways. Morrow *et al.* (2004) noted that warm-core eddies found west of Western Australia move north of westward, while cold-core eddies move south of westward, in accordance with the nonlinear mechanism of Cushman-Roisin (1994). The anticyclonic eddies cross a topographic ridge near 100°E, and a tendency for their westward movement to stall there can be seen in Morrow *et al.,* Figure 1. The cyclonic eddies miss this ridge. Morrow *et al.* (2003) also note that the eddies extend down to at least 2000 db, so they may well be experiencing topographic steering as in the ACC (e.g. Hughes, 2005). Whether or not such eddies result in departure from Sverdrup balance on longterm needs to be clarified, but at least the eddies display nonlinear behavior and interaction with the bottom; so they seem to provide a useful clue in searching for a mechanism for disposing of any vorticity imbalances, as northward flow from the ACC boundary relaxes back towards Sverdrup balance. In particular, the enhanced flow seen in the "meridional tip jet" carrying the Flinders Current westward and then northward in Figure 2 has enhanced gradients of Q, i.e. of APE, across it; so it probably has an enhanced

Eady growth rate. Perhaps its northward path, following ambient Sverdrup flow, is part of the means by which such regions of enhanced flow relax towards Sverdrup balance.

Northwest of the South African tip, the Benguela Current extends northwestward in Figures 2a–c that is much stronger than its (purely Sverdrup) equivalent in Figures 2c–e. It has features in common with the real-life "zonal jets" just discussed. This extra flow passes through a region of very intense eddy activity known as the "Cape Cauldron" (Boebel *et al.,* 2003); see Figure 2 of Morrow *et al.* (2004). It may be steered northward by an eddy-generated vorticity transfer to the bottom.

8. Summary of comparison of G89 theory with hydrographic observations

Direct, hydrographic measurements of the Q field relative to 1500 db, which provides geostrophic balance for depth-integrated flow in the top 1500 m relative to an assumed "depth of no motion" at 1500 m, have been compared with estimates from the G89 wind-driven model. The newer hydrographic and wind products used allows a more detailed examination than was given in G89. Because two independent sources of wind stresses have been used, and three of hydrography, it is possible to identify some failures of the G89 rules with some certainty. G89 showed that Q values "teleconnect" in quite subtle ways. For example, because of near-cancellation in two wind path integrals, the difference between Q along the east Atlantic relative to the southeast Pacific (Fig. 5) is mainly needed to provide geostrophic balance for the Coriolis force acting on the Indonesian Throughflow, as it crosses the latitude of the South African meridional tip.

Corresponding to each zonal jet of Figure 3, there is a "meridional tip jet," or MTJ, that starts from the same place—the meridional tip of some land mass. However, inspection of Figure 2—especially Figure 2c, with the greatest data density—reveals one type of consistent departure from Sverdrup balance. The figure shows that most MTJ paths are not zonal; north of the ACC boundary (as defined above) they mostly tend to follow contours of ambient Sverdrup flow of Figure 3.

Also, while Eq. (2) is a useful broad guide to Q along all eastern boundaries except New Zealand (Fig. 5), there are local departures with horizontal length scales of order one thousand kilometers, in which depth-integrated flows of as much as 5 Sverdrup on or off the shelf are unaccounted for by (2). It is possible that this is simply a function of the scarcity of Argo data near some coastlines. Surprisingly, G89 also provides useful estimates of the "depth-integrated pressure heads" driving the major western boundary currents against friction.

In the open ocean, it seems likely that the departures of Q patterns from Sverdrup prediction may (at least in the cases examined) be due either to LPS-style advection due to currents extending deeper than 1500 m, or to nonlinear interactions among the vigorous eddies often surrounding these departures from Sverdrup balance. In either case, the output of an eddy-resolving Ocean General Circulation Model (OGCM) may spontaneously generate these features; the dynamics causing these departures from Sverdrup balance could then be identified "simply" by diagnosing the output of such OGCMs. This has been

done successfully in the equatorial Pacific Ocean (e.g. Kessler *et al.,* 2003; Brown *et al.,* 2010) and the north Indian Ocean (Hu and Godfrey, 2007). However, eddies have much larger lengthscales in these low latitudes, so these authors obtained adequate eddy resolution from relatively coarse OGCMs.

Means of improving the quality of maps of both Q and Q_W exist. For Q, Ridgway and Dunn (2009) have prepared a climatology for Australasian waters, using the tight correlation between surface dynamic height, and temperature and salinity anomalies at individual depths, with altimeter sea level to effectively increase the number of hydrographic observations considerably. For Q_W, a version of the ERS winds calibrated against Fairall *et al.* (2003) drag coefficients should reduce the small but perceptible difference in amplitude between Figure 2 and Figure 3b.

Acknowledgements. The first author thanks CSIRO for providing him with office facilities for several years of work on this topic, via a CSIRO Post-Retirement Fellowship. Trevor McDougall, Gary Meyers, George Cresswell and David Griffin provided useful comments on earlier drafts, and Steve Rintoul's guidance to ACC literature has been invaluable. Billy Kessler went well beyond the call of duty in improving this paper, as part of the peer review process. George Veronis' encouragement of this project—and his suggestion to publish in the *Journal of Marine Research*—are also gratefully acknowledged.

APPENDIX

In this Appendix three island transports and seven differences in Q between meridional tips of land masses are expressed, via the rules given in Section 2, in terms of integrals of the long-path component of annual mean wind stress $\tau^{(l)}$ along particular paths.

Water volume is conserved according to those rules so that the component of the depth-integrated flowing perpendicularly to the left of the direction l along a path is given by ψ_l, where ψ is the volume transport streamfunction. The depth-integrated, longterm mean momentum equation in the longpath direction l is then:

$$gQ_l = \frac{\tau^{(l)}}{\rho} + f\psi_l \tag{8}$$

(8) is integrated below along ten paths, indicated by the letters next to path corners in Figure 1. Each path is composed of segments, of two kinds: segments following eastern ocean boundaries, along which $\psi_l = 0$; and zonal segments between two coastlines, for which Coriolis parameter f is constant. For these, the path integral of $f\psi_l$ is f times the difference in ψ between the two coastlines. The first three paths close around islands, so the path integral of Q_l vanishes, giving relations on island streamfunctions ψ_{NZ}, ψ_{Aust}, ψ_{Madag} along the coasts of New Zealand, Australasia, and Madagascar respectively. The remaining seven integrals determine the difference in Q between the southern tips of seven landmasses, and the point A on the South American coast. The formulae below use explicit values for the latitudes assumed in calculating the Table,

for the relevant meridional land mass tips. The results are, assuming the streamfunction is zero along all non-island coasts:

New Zealand streamfunction:

$$0 = \oint_{ADCBA} \frac{\tau^{(l)}}{\rho}\, dl + (f(34°S) - f(48°S))\psi_{NZ} \tag{9}$$

Australasian streamfunction:

$$0 = \oint_{AIHFEBA} \frac{\tau^{(l)}}{\rho}\, dl + f(0°S)*\psi_{Aust} - f(44°S)*(\psi_{Aust} - \psi_{NZ}) - f(48°S)*\psi_{NZ} \tag{10}$$

Madagascar streamfunction:

$$0 = \oint_{KJMLK} \frac{\tau^{(l)}}{\rho}\, dl + (f(12°S) - f(26°S))(\psi_{Madag} - \psi_{Aust}) \tag{11}$$

South tip B, New Zealand:

$$g*(Q(A) - Q(B)) = \int_{BA} \frac{\tau^{(l)}}{\rho}\, dl - f(48°S)*\psi_{NZ} \tag{12}$$

South tip F, Australasia:

$$g*(Q(A) - Q(F)) = \int_{ABEF} \frac{\tau^{(l)}}{\rho}\, dl + f(44°S)*(\psi_{NZ} - \psi_{Aust}) - f(48°S)*\psi_{NZ} \tag{13}$$

South tip Q, Indonesia:

$$g*(Q(A) - Q(Q)) = \int_{QNHIA} \frac{\tau^{(l)}}{\rho}\, dl + f(8°S)*\psi_{Aust} - f(0°S)*\psi_{Aust} \tag{14}$$

South tip R, India-Sri Lanka:

$$g*(Q(A) - Q(R)) = \int_{ROQNHIA} \frac{\tau^{(l)}}{\rho}\, dl + f(8°S)*\psi_{Aust} - f(0°S)*\psi_{Aust} \tag{15}$$

South tip K, Madagascar:

$$g^*(Q(A) - Q(K)) = \int_{KJHIA} \frac{\tau^{(l)}}{\rho}\, dl + f(26°S)^*(\psi_{Aust} - \psi_{Madag}) - f(0°S)^*\psi_{Aust} \qquad (16)$$

South tip X, South Africa:

$$g^*(Q(A) - Q(X)) = \int_{XGHIA} \frac{\tau^{(l)}}{\rho}\, dl + f(36°S)^*\psi_{Aust} - f(0°S)^*\psi_{Aust}. \qquad (17)$$

Once these calculations are complete, Q at all other eastern coastal points are obtained from Q at these seven points, by integrating (2) northwards. Q along western boundaries is obtained by use of (3), with appropriate choice of coastal streamfunction values.

REFERENCES

Anderson, D. L. T. and A. E. Gill. 1975. Spinup of a stratified ocean, with applications to upwelling. Deep-Sea Res. (Oceanogr. Abs.), *22,* 583–596.

Bentamy,A., K. B. Katsaros, A. M. Mestas-Nunez, W. M. Drennan, H. Roquet and E. B. Forde. 2003. Satellite estimates of wind speed and latent heat flux over the global oceans. J. Clim., *16,* 637–656.

Boebel, O., J. Lutjeharms, C. Schmid, W. Zenk, T. Rossby and C. Barron. 2003. The Cape Cauldron: A regime of turbulent inter-ocean exchange. Deep-Sea Res. II, *50,* 57–86.

Brown, J. N., J. S. Godfrey and S. E. Wijffels. 2010. Nonlinear effects of tropical instability waves on the Pacific. J. Phys. Oceanogr., *40,* 381–393.

Bunker, A. F. 1976. Computations of surface energy flux and annual air-sea interaction cycles of the North Atlantic Ocean. Mon. Weath. Rev., *104,* 1122–1140.

Cushman-Roisin, B. 1994. Introduction to Geophysical Fluid Dynamics, Prentice-Hall, 320 pp.

Dunn, J. and K. R. Ridgway. 2002. Mapping ocean properties in regions of complex topography. Deep-Sea Res. I, *49,* 591–604.

Fairall, C. W., E. F. Bradley, J. E. Hare, A. A. Grachev and J. B. Edson. 2003. Bulk parameterization of air-sea fluxes: updates and verification for the COARE algorithm. J. Clim., *16,* 571–591.

Gill, A. E. 1982. Atmosphere–Ocean Dynamics, Academic Press, 662 pp.

Godfrey, J. S. 1989. A Sverdrup model of the depth-integrated flow for the world ocean allowing for island circulations. Geophys. Astrophys. Fluid Dyn., *45,* 89–119.

Godfrey,J. S. and Y. Masumoto. 1996. Diagnosing the mean strength of the Indonesian Throughflow in an ocean general circulation model. J. Geophys. Res., *104,* 7889–7896.

Gordon, A. L. 1986. Inter-ocean exchange of thermocline water. J. Geophys. Res., *91,* 5037–5046.

Heath, R. A. 1985. A review of the physical oceanography of the seas around New Zealand. New Zealand J. Mar. Freshwater Res., *19,* 79–124.

Hellerman, S. and M. Rosenstein. 1983. Normal monthly wind stress over the World Ocean with error estimates. J. Phys. Oceanogr., *13,* 1093–1104.

Hill, K. L., S. R. Rintoul, R. Coleman and K. R. Ridgway. 2008. Wind forced low frequency variability of the East Australia Current. Geophys. Res. Lett., *35,* L08602, doi:10.1029/2007GL032912.

Hu, R.-J. and J. S. Godfrey. 2007. Explorations of the annual mean heat budget of the tropical Indian Ocean, Part II: Studies with a simplified Ocean General Circulation Model. J. Clim., *20,* 3229–3248.

Hughes, C. W. 2005. The nonlinear vorticity balance of the Antarctic Circumpolar Current. J. Geophys. Res., *110,* C11008, doi:10.1029/2004JC002753.

Hughes C. W., M. S. Jones and S. Corcoran. 1998. Use of transient features to identify eastward currents in the Southern Ocean. J. Geophys. Res., *103,* 2929–2944.

Johnson, G. C. and H. L. Bryden. 1989. On the size of the Antarctic Circumpolar Current. Deep-Sea Res., *36,* 39–53.

Kessler, W. S., G. C. Johnson and D. W. Moore. 2003. Sverdrup and nonlinear dynamics of the Pacific Equatorial Currents. J. Phys. Oceanogr., *33,* 994–1008.

Levitus, S. 1982. Climatological Atlas of the World Ocean, NOAA Prof. Pap., *13,* U.S. Gov. Print. Off., Washington, D.C., 173 pp.

Levitus *et al.* 1998. World Ocean Database, Vol. 1, Introduction. NOAA Atlas NESDIS 18, U.S. Government Printing Office, Washington, D.C.

Luyten, J. R., J. Pedlosky and H. Stommel. 1983. The ventilated thermocline. J. Phys. Oceanogr., *13,* 292–309.

Middleton, J. F. and M. Cirano. 2002. A northern boundary current along Australia's southern shelves: The Flinders Current. J. Geophys. Res., *10,* 3129, doi:10.1029/2000JC00071.

Morrow, R., F. Birol, D. Griffin and J. Sudre. 2004. Divergent pathways of cyclonic and anti-cyclonic ocean eddies. Geophys. Res. Lett., *31,* L24311, doi:10.1029/2004GL020974.

Morrow, R., F. Fang, M. Fieux and R. Molcard. 2003. Anatomy of three warm-core Leeuwin Current eddies. Deep-Sea Res. II, *50,* 2229–2243.

O'Neill, L. W., D. B. Chelton and S. K. Esbenson. 2003. Observations of SST-Induced perturbations of the wind stress field over the Southern Ocean on seasonal timescales. J. Clim., *16,* 2340–2354.

Pedlosky, J., L. J. Pratt, M. A. Spall and K. R. Helfrich. 1997. Circulation around islands and ridges. J. Mar. Res., *55,* 1199–1251.

Qiu, B., S. Chen and W. S. Kessler. 2009. Source of the 70-day mesoscale variability in the Coral Sea and the North Fiji Basin. J. Phys. Oceanogr., *39,* 404–420.

Ridgway K. R., J. R. Dunn and J. L. Wilkin. 2002. Ocean interpolation by four-dimensional least squares—Application to the waters around Australia, J. Atmos. Ocean. Tech., *19,* 1357–1375.

Ridgway, K. R. and J. R. Dunn. 2010. Using satellite altimetry to correct mean temperature and salinity fields derived from Argo floats in the ocean regions around Australia. Deep-Sea Res. I, *57,* 1137–1151.

Rintoul, S. R. and S. Sokolov. 2001. Baroclinic transport variability of the Antarctic Circumpolar Current south of Australia (WOCE repeat section SR3). J. Geophys. Res., 106C, 2815–2832.

Smith, S. D. 1988. Coefficients for sea surface wind stress, heat flux and wind profiles as a function of wind speed and temperature. J. Geophys. Res., *93,* 15467–15472.

Stramma, L. and R. G. Peterson. 1990. The South Atlantic Current. J. Phys. Oceanogr., *20,* 846–859.

Sverdrup, H. 1947. Wind-driven currents in a baroclinic ocean, with application to the equatorial currents of the eastern Pacific. Proc. Nat. Acad. Sci. U.S.A., *33,* 318–326.

Sverdrup, H. U., M. H. Johnson and R. H. Fleming. 1942. The Oceans: Their Physics, Chemistry and General Biology, Prentice-Hall, 1087 pp.

Vivier, F. and C. Provost. 1999. Volume transport of the Malvinas Current: can the flow be monitored by Topex-Poseidon? J. Geophys. Res., *104, 21,* 105–21, 122.

Wajsowicz, R. C. 1993a. The circulation of the depth-integrated flow around an island with applications to the Indonesian Throughflow. J. Phys. Oceanogr., *23,* 1470–1484.

—— 1993b. A simple model of the Indonesian throughflow and its composition. J. Phys. Oceanogr., *23,* 2684–2703.

—— 1996. Flow of a western boundary current through multiple straits: An electrical circuit analogy for the Indonesian Throughflow and archipelago. J. Geophys. Res., *101,* 12295–12300.

Wells, N. T. and B. J. de Cuevas. 1995. Depth-integrated vorticity budget of the Southern Ocean from a general circulation model. J. Phys. Oceanogr., *25,* 2569–2582.

Williams, R. G., C. Wilson and C. W. Hughes. 2007. Ocean and atmosphere storm tracks: the role of eddy vorticity forcing. J. Phys. Oceanogr., *37,* 2267–2289.

Xie, S.-P., W. T. Liu, Q. Liu and M. Nonaka. 2001. Far-reaching effects of the Hawaiian Islands on the Pacific Ocean-Atmosphere system. Science, *292,* 2057–2060, doi:10.1126/science.1059781.

Received: *26 February, 2010;* revised: *10 June, 2010.*